

## Slow-Time MIMO-FMCW Automotive Radar Detection With Imperfect Waveform Separation

Wang, Pu; Boufounos, Petros T.; Mansour, Hassan; Orlik, Philip V.

TR2020-039 April 11, 2020

### Abstract

This paper considers object detection in the case of imperfect waveform separation, in the context of automotive radars with a slow-time MIMO-FMCW signaling scheme. We develop an explicit signal model that accounts for waveform separation residuals and propose a Kronecker subspace-based object detector in the framework of generalized likelihood ratio test (GLRT). Our exact theoretical analysis under both hypotheses shows that the proposed detector holds the desired property of constant false alarm rate (CFAR). Numerical simulations validate our proposed object detection scheme.

*IEEE International Conference on Acoustics, Speech, and Signal Processing (ICASSP)*

This work may not be copied or reproduced in whole or in part for any commercial purpose. Permission to copy in whole or in part without payment of fee is granted for nonprofit educational and research purposes provided that all such whole or partial copies include the following: a notice that such copying is by permission of Mitsubishi Electric Research Laboratories, Inc.; an acknowledgment of the authors and individual contributions to the work; and all applicable portions of the copyright notice. Copying, reproduction, or republishing for any other purpose shall require a license with payment of fee to Mitsubishi Electric Research Laboratories, Inc. All rights reserved.



# SLOW-TIME MIMO-FMCW AUTOMOTIVE RADAR DETECTION WITH IMPERFECT WAVEFORM SEPARATION

Pu Wang, Petros Boufounos, Hassan Mansour, and Philip V. Orlik

Mitsubishi Electric Research Laboratories (MERL)  
Cambridge, MA 02139, USA

## ABSTRACT

This paper considers object detection in the case of imperfect waveform separation, in the context of automotive radars with a slow-time MIMO-FMCW signaling scheme. We develop an explicit signal model that accounts for waveform separation residuals and propose a Kronecker subspace-based object detector in the framework of generalized likelihood ratio test (GLRT). Our exact theoretical analysis under both hypotheses shows that the proposed detector holds the desired property of constant false alarm rate (CFAR). Numerical simulations validate our proposed object detection scheme.

**Index Terms**— Automotive radar, MIMO, frequency modulated continuous waveform (FMCW), detection.

## 1. INTRODUCTION

Automotive radar is rapidly becoming an indispensable component in ADAS (advanced driver assistance systems) and emerging autonomous driving applications. Along with ultrasonic, camera and LIDAR sensors, it assists in sensing and understanding the environment in a variety of weather conditions, with affordable cost. Particularly, automotive radar provides direct measurement of radial velocities, long operating range, small size at millimeter or subterahertz frequency bands, and high spatial resolution [1, 2].

This has led to the development of new signaling schemes to handle mutual interference, such as phase-modulated continuous wave (PMCW) and stepped-carrier OFDM. Among these schemes, frequency modulated continuous waveform (FMCW) is overwhelmingly preferred in practice for its simple transceiver architecture, low sampling rate requirements, and its ability to harness a wide frequency bandwidth.

At the same time, to increase the spatial resolution, multiple-input multiple-output (MIMO) radars have been incorporated into automotive radars for expanded virtual array aperture [3–12]. In general, MIMO radars can be realized in either the time domain (TDMA) or the waveform domain. In highly dynamical environments such as highways, the waveform-coded MIMO is preferred. Compared to fast-time MIMO radars, requiring multiplying orthogonal codes on the sample-to-sample basis, slow-time MIMO radars with orthogonal codes only on the pulse-to-pulse basis appear to be a more cost-efficient solution for hardware implementation [5].

The existing literature mostly assumes perfect waveform separation at each receiver, achieved by applying corresponding orthogonal codes at the transmitters. However, such ideal waveform separation is impossible across all Doppler frequencies and time delays [13–20]. Therefore, the effect of waveform residuals has to be considered for automotive object detection. Detection sensitivity with respect to changes in cross-correlation levels was analyzed in the case of distributed MIMO radars [15, 18]. In [17] and [20], robust

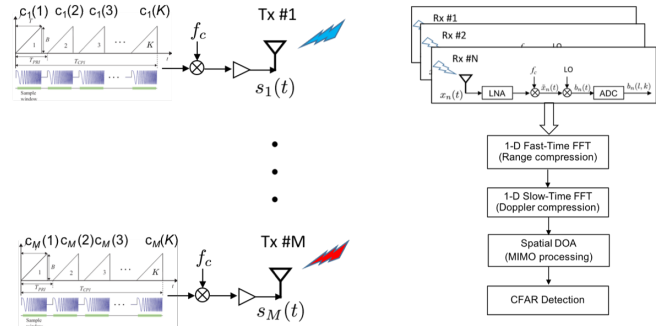


**Fig. 1.** The slow-time MIMO-FMCW automotive radar architecture. On the left, a sequence of FMCW pulses with orthogonal slow-time (pulse) codes are sent from  $M$  transmitting antennas while, on the right, each of  $N$  receivers uses the same source FMCW waveform to sample the beat signal followed by range-doppler processing and slow-time waveform separation for spatial MIMO detection.

target detectors were proposed to explicitly account for waveform residuals in fast-time waveform-coded distributed MIMO radars.

In this paper, we account for such imperfect waveform separation effect into the context of slow-time MIMO-FMCW automotive radars. In particular, we develop an explicit signal model that accounts for waveform separation residuals. Following that, we formulate object detection as a binary hypothesis testing where the waveform residuals only appear in the alternative hypothesis when the target of interest is present. According to the developed signal model, a Kronecker subspace-based object detector is proposed according to the principle of generalized likelihood ratio test (GLRT). We provide exact theoretical analysis under both hypotheses and we prove that the proposed detector holds the desired property of *constant false alarm rate* (CFAR).

## 2. WAVEFORM RESIDUALS FOR SLOW-TIME MIMO-FMCW AUTOMOTIVE RADAR

As shown in Fig. 1, a slow-time MIMO-FMCW automotive radar uses  $M$  transmitters sending  $K$  coded FMCW pulses

$$s_m(t) = \sum_{k=0}^{K-1} c_m(k) s_p(t - kT_{\text{PRI}}) e^{j2\pi f_c t}, \quad (1)$$

where  $m$  and  $k$  are, respectively, the indices for the transmitter and pulse,  $c_m(k)$  is the orthogonal code for the  $k$ -th pulse at the  $m$ -th transmitter,  $T_{\text{PRI}}$  is the pulse repetition interval (PRI),  $f_c$  is the carrier

frequency (e.g.,  $f_c = 79$  GHz), and  $s_p(t)$  is the baseband FMCW waveform

$$s_p(t) = \begin{cases} e^{j\pi\beta t^2} & 0 \leq t \leq T \\ 0 & \text{otherwise,} \end{cases} \quad (2)$$

with  $\beta$  denoting the chirp rate and  $T$  the pulse duration. The bandwidth of the FMCW waveform is  $B = \beta T$ . The baseband waveform is repeated at each antenna before being multiplied by orthogonal codes  $c_m(k)$ , e.g., Hadamard code.

For an object at a distance of  $R_0$  with a radial velocity  $v_t$ , the round-trip propagation delay from the  $m$ -th transmitting antenna to the  $n$ -th receiving antenna is

$$\tau_{mn}(t) = 2\frac{R_0 + vt}{c} + m\frac{d_t \sin(\theta_t)}{c} + n\frac{d_r \sin(\theta_r)}{c}, \quad (3)$$

where  $d_{t/r}$  and  $\theta_{t/r}$  are the inter-element spacing and azimuthal angle for the transmitting and receiving antennas, respectively. We assume colocated radars and the far field approximation, i.e.,  $\theta_r = \theta_t = \theta$ .

In the presence of an object at angle  $\theta$ , the  $n$ -th receiver in Fig. 1 receives the baseband signal (after the carrier frequency down-conversion)

$$\tilde{x}_n(t) \approx \tilde{\alpha} \sum_m s_m(t - \tau_0) e^{-j2\pi f_c \frac{2vt}{c}} e^{-j2\pi(md_t + nd_r) \frac{\sin(\theta)}{\lambda}}, \quad (4)$$

where  $\tau_0 = 2R_0/c$  and  $\lambda = c/f_c$ . We assume that  $s(t - \tau_{mn}) \approx s(t - \tau_0)$  and  $\tilde{\alpha}$  absorbs constant phase factors. The signals at all receivers are mixed with the source chirp to generate the analog beat signal as  $b_n(t) = \tilde{x}_n(t) \sum_k s_p^*(t - kT_{\text{PRI}})$

$$b_n^{(k)}(t) = \tilde{\alpha} \sum_m c_m(k) e^{-j2\pi\beta\tau_0(t - kT_{\text{PRI}})} e^{-j2\pi f_c(2vt/c)} e^{-j2\pi(md_t + nd_r) \frac{\sin(\theta)}{\lambda}}, \quad (5)$$

where  $\tilde{\alpha}$  absorbs additional phase terms. The analog beat signal is then sampled at  $t = kT_{\text{PRI}} + l\Delta T$ , where  $\Delta T$  and  $T_{\text{PRI}}$  are, respectively, the fast-time and slow-time sampling intervals

$$b_n(l, k) = \tilde{\alpha} \sum_m c_m(k) e^{-j2\pi f_r l} e^{-j2\pi f_d k} e^{-j2\pi(f_s^t m + f_s^r n)}, \quad (6)$$

where  $f_r = (\beta\tau_0 + 2f_c v/c) \Delta T$  is normalized temporal (fast-time) frequency,  $f_d = 2f_c T_{\text{PRI}} v/c$  is the normalized Doppler (slow-time) frequency, and  $f_s^{t/r}$  is the normalized spatial frequency at the transmitting and receiving antennas ( $f_s^t$  is usually different from  $f_s^r$  due to different Tx/Rx spacings). In other words, the beat signal at the  $n$ -th receiver is the sum of object responses originated from all transmitted waveforms, coded using  $c_m(k)$ .

Due to limited computational resources, typically objects are first detected in the range-Doppler  $(l, k)$  domain, before the slow-time MIMO waveform separation. Once targets are detected, their azimuthal angle is estimated using waveform separation in the slow-time domain with identified Doppler frequency  $\hat{f}_d$  to compensate the modulation. Specifically, one can separate the received waveform in the slow-time domain as

$$b_{in}(l) = \sum_k c_i(k) b_n(l, k) e^{j2\pi \hat{f}_d k}, \quad i = 1, \dots, M. \quad (7)$$

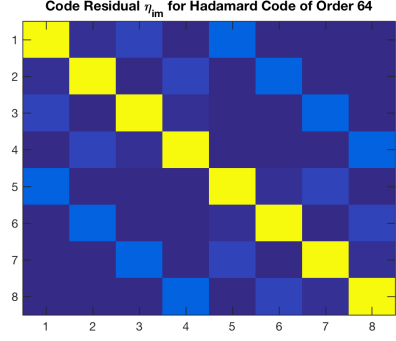


**Fig. 2.** The code residual  $\eta_{im}$  for a Hadamard code of order 64 with a normalized Doppler frequency mismatch of  $\Delta f_d = 0.01$ . The first  $M = 8$  columns of the Hadamard matrix are used for the orthogonal code  $\{c_m(k), m = 1, \dots, M, k = 1, \dots, K\}$ .

As a result, one can form the MIMO virtual array over all transmitting elements  $i$  and receiving elements  $n$ . For a given range cell  $l$ , the waveform separation gives the Tx-Rx virtual array as

$$b_{in}(l) = \tilde{\alpha} e^{-j2\pi f_r l} e^{-j2\pi f_s^r n} \left( e^{-j2\pi f_s^t i} \eta_{ii} \right) + \tilde{\alpha} e^{-j2\pi f_r l} e^{-j2\pi f_s^r n} \left( \sum_{m \neq i} e^{-j2\pi f_s^t m} \eta_{im} \right) \quad (8)$$

where  $\eta_{im} = \sum_k c_m(k) c_i(k) e^{-j2\pi \Delta f_d k}$  measures the code residuals. Equation (8) reveals that, after slow-time waveform separation, we can form a virtual array of  $MN$  elements for each detected object and identify its spatial extent in the Tx-Rx element  $(i, n)$  domain. The waveform at each virtual element  $(i, n)$  consists of two components: the object signal, weighted by  $\eta_{ii}$ , and the residual signal, a weighted sum of  $M - 1$  components weighted by  $\eta_{im}$ . If  $\Delta f_d = 0$ , one can have perfect waveform separation  $b_{in}(l) = K \tilde{\alpha}_{in} e^{-j2\pi(f_s^t i + f_s^r n)} e^{-j2\pi f_r l}$  since  $\eta_{ii} = K$  while  $\eta_{im} = 0$ . In practice, however, a small mismatch in the Doppler domain may lead to significant leakage in the separated waveform. Figure 2 shows an example of the code residual  $\eta_{im}$  for a MIMO radar with  $M = 8$  transmitting elements and  $K = 64$  pulses using a Hadamard code of order 64 for slow-time waveform separation and a normalized Doppler frequency mismatch  $\Delta f_d = 0.01$ . The spectrum leakage, present in the off-diagonal elements,  $\eta_{im}, i \neq m$ , is severe.

For each range cell  $l$ , we define the steering vector by stacking all  $MN$  virtual elements, noting that  $\eta_{ii} = \eta$

$$\mathbf{b}(l) \approx \tilde{\alpha} \mathbf{s}(f_s^r) \otimes \mathbf{s}(f_s^t) + \mathbf{s}(f_s^r) \otimes (\mathbf{H}(f_s^t) \boldsymbol{\eta}) \quad (9)$$

where  $\tilde{\alpha}$  absorbs additional phase terms,  $\mathbf{b}(l) \in \mathbb{C}^{MN \times 1}$ ,  $\mathbf{s}(f_s^t) = [1, \dots, e^{-j2\pi f_s^t (M-1)}]^T$ ,  $\mathbf{s}(f_s^r) = [1, \dots, e^{-j2\pi f_s^r (N-1)}]^T$  and the subspace matrix  $\mathbf{H} \in \mathbb{C}^{M \times d}$  is

$$\mathbf{H}(f) = \begin{bmatrix} e^{-j2\pi f} & e^{-j2\pi f 2} & \dots & e^{-j2\pi f d} \\ 1 & e^{-j2\pi f 2} & \dots & e^{-j2\pi f d} \\ \vdots & \vdots & \ddots & \vdots \\ 1 & e^{-j2\pi f 1} & \dots & e^{-j2\pi f (d-1)} \end{bmatrix}, \quad (10)$$

with  $d$  denoting the subspace dimension that is related to the off-diagonal leakage of  $\eta_{im}$  in Fig. 2 and  $\boldsymbol{\eta}$  is the corresponding subspace coefficient. It is worth noting that (8) implies that the residual

subspace dimension can be up to  $M - 1$ . In practice, given the orthogonal code at the transmitter and the maximum range of Doppler mismatch, one can assess the pattern of  $\eta_{im}$  and use the number of significant code residuals to determine the subspace dimension  $d$ .

### 3. SPATIAL MIMO DETECTION

Object detection and spatial localization can be formulated as a binary hypothesis testing problem in the presence of the residual waveform. Thus, we use the GLRT to develop a Kronecker subspace-based detector.

#### 3.1. Hypothesis Testing

To formulate the binary hypothesis test we consider the target signal, its residual signal due to imperfect waveform separation, and the disturbance, including the background clutter, jamming signals and thermal noise. More specifically,

$$\begin{aligned} H_0 : \quad & \mathbf{x}(l) = \mathbf{w}(l), \\ H_1 : \quad & \mathbf{x}(l) = \alpha_l \mathbf{s} \otimes \mathbf{t} + \mathbf{s} \otimes (\mathbf{H}\boldsymbol{\eta}_l) + \mathbf{w}(l), \end{aligned} \quad (11)$$

where the disturbance is assumed to be Gaussian distributed with zero mean and covariance matrix  $\mathbf{R}$ , i.e.,  $\mathbf{w} \sim \mathcal{CN}(\mathbf{0}, \sigma^2 \mathbf{R})$ . If  $\mathbf{R}$  is unknown, one can estimate it from training signals at neighboring range cells. The receiving and transmitting steering vectors  $\{\mathbf{s}, \mathbf{t}\}$ , with corresponding dimension  $N$  and  $M$ , respectively, and the subspace matrix  $\mathbf{H}$  are assumed known, following our signal model.

#### 3.2. Proposed Spatial MIMO Detection

With known  $\mathbf{R}$  or estimated  $\hat{\mathbf{R}}$ , the signal is whitened using  $\mathbf{y} = \mathbf{R}^{-1/2} \mathbf{x}$  mapping detection to following binary hypothesis test:

$$\begin{aligned} H_0 : \quad & \mathbf{y} \sim \mathcal{CN}(\mathbf{0}, \sigma^2 \mathbf{I}), \\ H_1 : \quad & \mathbf{y} \sim \mathcal{CN}(\mathbf{R}^{-1/2}(\mathbf{s} \otimes (\alpha \mathbf{t} + \mathbf{H}\boldsymbol{\eta})), \sigma^2 \mathbf{I}). \end{aligned} \quad (12)$$

For simplicity, we assume that  $\mathbf{R} = \mathbf{R}_N \otimes \mathbf{R}_M$ . As a result,  $\tilde{\mathbf{s}} = \mathbf{R}_N^{-1/2} \mathbf{s}$ ,  $\tilde{\mathbf{t}} = \mathbf{R}_M^{-1/2} \mathbf{t}$ ,  $\tilde{\mathbf{H}} = \mathbf{R}_M^{-1/2} \mathbf{H}$ , and  $\tilde{\mathbf{w}} = \mathbf{R}^{-1/2} \mathbf{w}$ . Note that the following derivations apply to a more general  $\mathbf{R}$ .

Subsequently, the GLRT can be derived as the ratio of maximized likelihoods under both hypotheses

$$T = \frac{\max_{\alpha, \boldsymbol{\eta}, \sigma^2} f_1(\mathbf{y} | \alpha, \boldsymbol{\eta}, \sigma^2)}{\max_{\sigma^2} f_0(\mathbf{y} | \sigma^2)}, \quad (13)$$

where  $T$  is the test statistic, and  $f_0(\mathbf{y} | \sigma^2)$  and  $f_1(\mathbf{y} | \alpha, \boldsymbol{\eta}, \sigma^2)$  are, respectively, the likelihood functions of the whitened signal

$$\begin{aligned} f_0(\mathbf{y} | \sigma^2) &= \frac{e^{-\frac{1}{\sigma^2} \mathbf{y}^H \mathbf{y}}}{(\pi \sigma^2)^{MN}} \\ f_1(\mathbf{y} | \alpha, \boldsymbol{\eta}, \sigma^2) &= \frac{e^{-\frac{1}{\sigma^2} \|\mathbf{y} - \tilde{\mathbf{s}} \otimes (\alpha \tilde{\mathbf{t}} + \tilde{\mathbf{H}}\boldsymbol{\eta})\|^2}}{(\pi \sigma^2)^{MN}}. \end{aligned} \quad (14)$$

By differentiating  $\ln f_1(\mathbf{y} | \alpha, \boldsymbol{\eta}, \sigma^2)$  w.r.t.  $\sigma^2$  and setting to zero, the ML estimate of  $\sigma^2$  under  $H_1$

$$\hat{\sigma}^2 = \frac{1}{MN} \|\mathbf{y} - \tilde{\mathbf{s}} \otimes (\alpha \tilde{\mathbf{t}} + \tilde{\mathbf{H}}\boldsymbol{\eta})\|^2. \quad (15)$$

Then the ML estimate of the remaining parameters  $\boldsymbol{\beta} = [\alpha, \boldsymbol{\eta}^T]^T$  can be determined by minimizing the following cost function

$$\|\mathbf{y} - \tilde{\mathbf{s}} \otimes (\tilde{\mathbf{H}}\boldsymbol{\beta})\|^2 \quad (16)$$

where  $\tilde{\mathbf{H}} = [\tilde{\mathbf{t}}, \tilde{\mathbf{H}}]$ . The ML estimate of  $\boldsymbol{\beta}$  follows:

$$\hat{\boldsymbol{\beta}} = \left[ (\tilde{\mathbf{s}}^H \tilde{\mathbf{s}})^{-1} \tilde{\mathbf{s}}^H \otimes (\tilde{\mathbf{H}}_t^H \tilde{\mathbf{H}}_t)^{-1} \tilde{\mathbf{H}}_t^H \right] \mathbf{y}. \quad (17)$$

Substituting  $\hat{\boldsymbol{\beta}}$  back to the cost function, we have

$$\begin{aligned} \|\mathbf{y} - \tilde{\mathbf{s}} \otimes (\tilde{\mathbf{H}}_t \hat{\boldsymbol{\beta}})\|^2 &= \left\| \mathbf{y} - \tilde{\mathbf{s}} \otimes \left[ ((\tilde{\mathbf{s}}^H \tilde{\mathbf{s}})^{-1} \tilde{\mathbf{s}}^H \otimes \mathbf{P}_{\tilde{\mathbf{H}}_t}) \mathbf{y} \right] \right\|^2 \\ &= \|\mathbf{y} - (\mathbf{P}_{\tilde{\mathbf{s}}} \otimes \mathbf{P}_{\tilde{\mathbf{H}}_t}) \mathbf{y}\|^2 = \mathbf{y}^H \mathbf{P}_{\tilde{\mathbf{s}} \otimes \tilde{\mathbf{H}}_t}^\perp \mathbf{y} \end{aligned}$$

where we use the Kronecker product property that  $(\mathbf{A} \otimes \mathbf{B})(\mathbf{C} \otimes \mathbf{D}) = (\mathbf{A}\mathbf{C}) \otimes (\mathbf{B}\mathbf{D})$ , and  $\mathbf{P}_{\tilde{\mathbf{s}}}^\perp = \mathbf{I} - \mathbf{A}(\mathbf{A}^H \mathbf{A})^{-1} \mathbf{A}^H = \mathbf{I} - \mathbf{P}_{\mathbf{A}}$ . As a result, the maximized likelihood under  $H_1$  is given by

$$\max_{\boldsymbol{\beta}, \sigma^2} f_1(\mathbf{y} | \boldsymbol{\beta}, \sigma^2) = \left( \frac{\pi}{MN} \mathbf{y}^H \mathbf{P}_{\tilde{\mathbf{s}} \otimes \tilde{\mathbf{H}}_t}^\perp \mathbf{y} \right)^{-MN}. \quad (18)$$

Similarly, under  $H_0$ , we have  $\max_{\sigma^2} f_0(\mathbf{y} | \sigma^2) = \left( \frac{\pi}{MN} \mathbf{y}^H \mathbf{y} \right)^{-MN}$ .

Taking the  $(MN)$ -th root, the GLRT in (13) is equivalent to

$$T = \frac{\mathbf{y}^H \mathbf{y}}{\mathbf{y}^H \mathbf{P}_{\tilde{\mathbf{s}} \otimes \tilde{\mathbf{H}}_t}^\perp \mathbf{y}} \rightarrow T' = T - 1 = \frac{\mathbf{y}^H \mathbf{P}_{\tilde{\mathbf{s}} \otimes \tilde{\mathbf{H}}_t} \mathbf{y}}{\mathbf{y}^H \mathbf{P}_{\tilde{\mathbf{s}} \otimes \tilde{\mathbf{H}}_t}^\perp \mathbf{y}} \quad (19)$$

In other words, the GLRT statistic is equivalent to the ratio of the energy of the whitened signal projected onto a subspace and its orthogonal complement, where the subspace is spanned by the Kronecker product of the column space of whitened transmitting steering vector  $\tilde{\mathbf{s}}$  and the whitened subspace  $\tilde{\mathbf{H}}_t$  for the waveform residuals.

#### 3.3. Theoretical Performance Analysis

We first define  $T_{\text{num}} = \mathbf{y}^H \mathbf{P}_{\tilde{\mathbf{s}} \otimes \tilde{\mathbf{H}}_t} \mathbf{y}$  and  $T_{\text{den}} = \mathbf{y}^H \mathbf{P}_{\tilde{\mathbf{s}} \otimes \tilde{\mathbf{H}}_t}^\perp \mathbf{y}$  and start with the following two lemmas.

*Lemma 1:* Under hypothesis  $H_0$ , the numerator and denominator have the following distributions [21, 22]

$$\frac{2}{\sigma^2} T_{\text{num}} = \frac{2}{\sigma^2} \sum_{n=1}^d |\tilde{w}_n|^2 \sim \chi_{2d}^2 \quad (20)$$

$$\frac{2}{\sigma^2} T_{\text{den}} = \frac{2}{\sigma^2} \sum_{n=d+1}^{MN} |\tilde{w}_n|^2 \sim \chi_{2(MN-d)}^2, \quad (21)$$

where  $\tilde{w}_n$  is the  $n$ -th element of the whitened noise  $\tilde{\mathbf{w}}$  and we have used the fact that the projection matrix  $\mathbf{P}_{\mathbf{A}}$  can be decomposed as  $\mathbf{P}_{\mathbf{A}} = \mathbf{Q} \text{diag}\{1, \dots, 1, 0, \dots, 0\} \mathbf{Q}^H$  with  $\mathbf{Q}$  containing corresponding eigenvectors and  $d$  non-zeros eigenvalues. Then the GLRT statistic is a ratio of two independent central Chi-square distributions with  $2d$  and  $2(MN - d)$  degrees of freedom. As a result,

$$\frac{(MN - d)}{d} T' \sim F_{2d, 2(MN-d)}, \quad \text{under } H_0, \quad (22)$$

where  $F_{v_1, v_2}$  is a central  $F$ -distribution with degrees of freedom  $v_1$  and  $v_2$ .

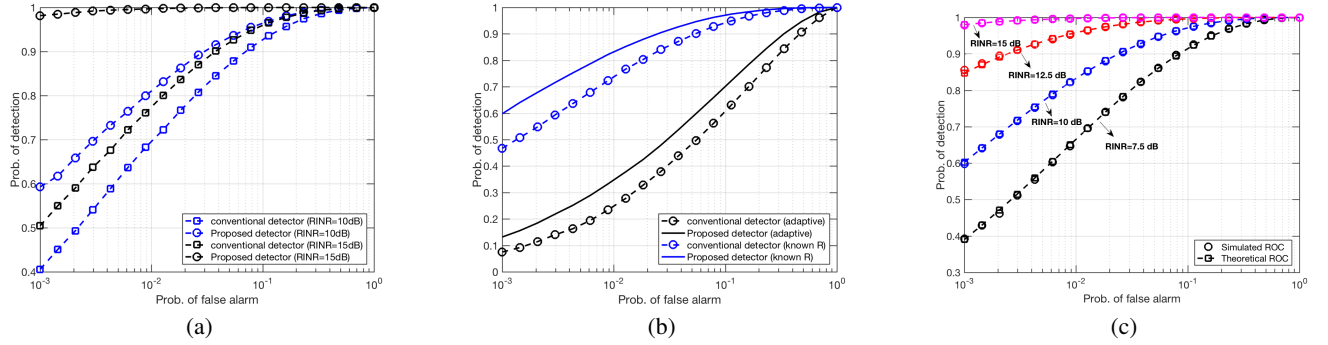


**Fig. 3.** (a) The receiver operating characteristic (ROC) curve under two levels of waveform separation residuals when  $\text{SINR} = 10$  dB. (b) Performance comparison of two object detectors in scenarios of clairvoyant (known  $\mathbf{R}$ ) and adaptive (unknown  $\mathbf{R}$ ) detection. (c) Performance validation of theoretical (squares with dashed lines) ROC curves with Monte-Carlo results (circles) at various RINRs when  $\text{SINR} = 10$  dB.

*Lemma 2:* Under hypothesis  $H_1$ , the numerator and denominator have the following distributions [21, 22]

$$\frac{2}{\sigma^2} T_{\text{num}} = \frac{2}{\sigma^2} \sum_{n=1}^d |\tilde{\zeta}_n|^2 \sim \chi_{2d}^2(\lambda) \quad (23)$$

$$\frac{2}{\sigma^2} T_{\text{den}} = \frac{2}{\sigma^2} \sum_{n=d+1}^{MN} |\tilde{\zeta}_n|^2 \sim \chi_{2(MN-d)}^2. \quad (24)$$

where the non-centrality parameter is  $\lambda = 2(\tilde{\mathbf{s}}^H \tilde{\mathbf{s}})(\boldsymbol{\beta}^H \tilde{\mathbf{H}}^H \tilde{\mathbf{H}} \boldsymbol{\beta})/\sigma^2$ . Then the GLRT statistic is a ratio of a non-central Chi-square random variable with  $2d$  degrees of freedom and noncentrality parameter  $\lambda$  to an independent central Chi-square random variable with  $2(MN - d)$  degrees of freedom. Therefore, we have

$$\frac{(MN - d)}{d} T' \sim F_{2d, 2(MN-d)}(\lambda), \text{ under } H_1, \quad (25)$$

where  $F_{v_1, v_2}(\lambda)$  is a non-central  $F$ -distribution with degrees of freedom  $v_1$  and  $v_2$  and non-centrality parameter  $\lambda$ .

Given the probabilistic distributions of the GLRT, we can analytically compute the probabilities of detection and false alarm. More importantly, Lemma 1 implies that the GLRT is a *constant false alarm rate* (CFAR) detector.

#### 4. NUMERICAL EXAMPLES

To evaluate the performance of the proposed detector and compare the verify the theoretical performance analysis we performed extensive simulations. In all simulations, we define the signal-to-interference-plus-noise ratio (SINR) and residual-to-interference-plus-noise ratio (RINR) as

$$\text{SINR} = 2|\alpha|^2 (\mathbf{s}^H \mathbf{R}_N^{-1} \mathbf{s})(\mathbf{t}^H \mathbf{R}_M^{-1} \mathbf{t})/\sigma^2, \quad (26)$$

$$\text{RINR} = 2(\mathbf{s}^H \mathbf{R}_N^{-1} \mathbf{s})(\boldsymbol{\eta}^H \mathbf{H}^H \mathbf{R}_M^{-1} \mathbf{H} \boldsymbol{\eta})/\sigma^2 \quad (27)$$

where  $\mathbf{s}$  represents the steering vector corresponding to  $N = 16$  receivers,  $\mathbf{t}$  is the steering vector for  $M = 8$  transmitters, and the disturbance covariance matrix  $\mathbf{R}_{M/N}$  is given as  $[\mathbf{R}]_{\ell\kappa} = \rho^{|\ell-\kappa|}$  with  $\rho = 0.6$ . The detection performance is evaluated in terms of the receiver operating characteristic (ROC) by using Monte-Carlo trials. For performance comparison, we include the conventional MIMO detector which ignores the presence of waveform residuals.

#### 4.1. Detection Performance Evaluation

We first consider a case of known  $\mathbf{R}$  or  $\mathbf{R} = \mathbf{I}$ . In this case, the received signal  $\mathbf{x}$  and steering vectors  $\mathbf{t}$  and  $\mathbf{s}$  are pre-whitened first using  $\mathbf{R}^{-1/2}$  as shown in (12). When  $\text{SINR} = 10$  dB, Fig. 3 (a) shows the ROC performance of the conventional detector and the proposed detector under two levels of waveform residuals: 1)  $\text{RINR} = 10$  dB and 2)  $\text{RINR} = 15$  dB. The results confirm that, by exploiting the target residual, the detection performance can be improved. Besides, larger performance improvement can be achieved if the target residual component is stronger (i.e., with larger RINR). This observation is intuitive as the stronger the target residual, the larger the separation between the null and alternative hypotheses and, hence, the better detection performance.

Next, we quantify the performance loss due to the unknown  $\mathbf{R}$ . In this case, training signals  $\mathbf{x}(l)$  from nearby range bins  $l$  are used for adaptive object detection. Fig. 3 (b) shows, when  $\text{RINR} = 10$  dB and 2)  $\text{RINR} = 10$  dB, the ROC curves for both adaptive and clairvoyant (known  $\mathbf{R}$ ) schemes of both detectors. It clearly shows that the detection performance degrades for both detectors when the disturbance covariance matrix has to be estimated from training signals. It is also observed that, in the case of adaptive detection, the proposed detector still outperforms the conventional detector.

#### 4.2. Theoretical Performance Validation

Finally, we validate the theoretical performance analysis with Monte-Carlo simulation results. To compute theoretical ROC curves, we need to evaluate the inverse of the cumulative distribution function (CDF) of an  $F$ -distribution (e.g., `finv` in MATLAB) and the CDF of a noncentral  $F$ -distribution (e.g., `ncfcdf` in MATLAB). Fig. 3 (c) shows the simulated ROC curves under various RINRs ranging from 7.5 dB to 15 dB and corresponding theoretical performance from (22) and (25). It is seen that, for all considered scenarios, the theoretical performance agrees well with simulated ROC curves even at small probabilities of false alarm, e.g.,  $P_f = 0.001$ .

#### 5. CONCLUSIONS

We considered object detection for slow-time MIMO-FMCW automotive radars by accounting for the residual waveform. Under this model, we propose a Kronecker subspace detection in the GLRT framework and provide exact performance analysis under both null and alternative hypotheses. Simulation results confirm the effectiveness of the proposed detection.

## 6. REFERENCES

- [1] I. Bilik, O. Longman, S. Villeval, and J. Tabrikian, "The rise of radar for autonomous vehicles: Signal processing solutions and future research directions," *IEEE Signal Processing Magazine*, vol. 36, no. 5, pp. 20–31, Sep. 2019.
- [2] G. Hakobyan and B. Yang, "High-performance automotive radar: A review of signal processing algorithms and modulation schemes," *IEEE Signal Processing Magazine*, vol. 36, no. 5, pp. 32–44, Sep. 2019.
- [3] D. W. Bliss and K. W. Forsythe, "Multiple-input multiple-output (MIMO) radar and imaging: degrees of freedom and resolution," in *Proceedings of the 37th Asilomar Conference on Signals, Systems, and Computers*, Pacific Grove, CA, November 2003, vol. 1, pp. 54–59.
- [4] J. Li, P. Stoica, L. Xu, and W. Roberts, "On parameter identifiability of MIMO radar," *IEEE Signal Processing Letters*, vol. 14, no. 12, pp. 968–971, Dec 2007.
- [5] J. Li and P. Stoica, *MIMO Radar Signal Processing*, John Wiley & Sons, 2008.
- [6] Y. Yang and R. S. Blum, "Phase synchronization for coherent MIMO radar: Algorithms and their analysis," *IEEE Trans. on Signal Processing*, vol. 59, no. 11, pp. 5538–5557, Nov 2011.
- [7] P. Wang, H. Li, and B. Himed, "A parametric moving target detector for distributed MIMO radar in nonhomogeneous environment," *IEEE Trans. on Signal Processing*, vol. 61, no. 9, pp. 2282–2294, May 2013.
- [8] Y. Li, S. A. Vorobyov, and V. Koivunen, "Ambiguity function of the transmit beamspace-based MIMO radar," *IEEE Trans. on Signal Processing*, vol. 63, no. 17, pp. 4445–4457, Sep. 2015.
- [9] A. Aubry, A. De Maio, and Y. Huang, "MIMO radar beampattern design via PSL/ISL optimization," *IEEE Trans. on Signal Processing*, vol. 64, no. 15, pp. 3955–3967, Aug 2016.
- [10] P. Chen, L. Zheng, X. Wang, H. Li, and L. Wu, "Moving target detection using colocated MIMO radar on multiple distributed moving platforms," *IEEE Trans. on Signal Processing*, vol. 65, pp. 4670–4683, Sep. 2017.
- [11] J. Liu, J. Han, Z. Zhang, and J. Li, "Bayesian detection for MIMO radar in gaussian clutter," *IEEE Trans. on Signal Processing*, vol. 66, no. 24, pp. 6549–6559, Dec 2018.
- [12] X. Yu, G. Cui, J. Yang, L. Kong, and J. Li, "Wideband MIMO radar waveform design," *IEEE Transactions on Signal Processing*, vol. 67, no. 13, pp. 3487–3501, July 2019.
- [13] Y. I. Abramovich and G. J. Frazer, "Bounds on the volume and height distributions for the MIMO radar ambiguity function," *IEEE Signal Process. Lett.*, vol. 15, pp. 505–508, 2008.
- [14] F. Daum and J. Huang, "MIMO radar: snake oil or good idea?," *IEEE Aerosp. Electron. Syst. Mag.*, vol. 24, no. 5, pp. 8–12, May 2009.
- [15] M. Akcakaya and A. Nehorai, "MIMO radar sensitivity analysis for target detection," *IEEE Trans. Signal Process.*, vol. 59, no. 7, pp. 3241–3250, July 2011.
- [16] P. Wang, J. Fang, H. Li, and B. Himed, "Detection with target-induced subspace interference," *IEEE Signal Process. Lett.*, vol. 19, no. 7, pp. 403–406, July 2012.
- [17] P. Wang, H. Li, and B. Himed, "Moving target detection for distributed MIMO radar with imperfect waveform separation," in *2013 IEEE Radar Conference (RadarCon13)*, April 2013, pp. 1–5.
- [18] A. Zaibashi, "Invariant subspace detector in distributed multiple-input multiple output radar: geometry gain helps improving moving target detection," *IET Radar, Sonar Navigation*, vol. 10, no. 5, pp. 923–934, 2016.
- [19] T. Aittomaki and V. Koivunen, "Mismatched filter design and interference mitigation for MIMO radars," *IEEE Trans. on Signal Processing*, vol. 65, no. 2, pp. 454–466, Jan 2017.
- [20] P. Wang and H. Li, "Target detection with imperfect waveform separation in distributed MIMO radar," *IEEE Trans. on Signal Processing*, vol. 68, pp. 793–807, Jan. 2020.
- [21] L. L. Scharf and B. Friedlander, "Matched subspace detectors," *IEEE Transactions on Signal Processing*, vol. 42, no. 8, pp. 2146–2157, August 1994.
- [22] P. Wang, H. Li, and B. Himed, "Moving target detection using distributed MIMO radar in clutter with nonhomogeneous power," *IEEE Trans. on Signal Processing*, vol. 59, pp. 4809–4820, October 2011.